nature nanotechnology

LETTERS

PUBLISHED ONLINE: 13 JUNE 2016 | DOI: 10.1038/NNANO.2016.86

Tunable phonon-cavity coupling in graphene membranes

R. De Alba[1]*, F. Massel[2], I. R. Storch[1], T. S. Abhilash[1], A. Hui[3], P. L. McEuen[1,4], H. G. Craighead[3] and J. M. Parpia[1]

A major achievement of the past decade has been the realization of macroscopic quantum systems by exploiting the interactions between optical cavities and mechanical resonators[1–3]. In these systems, phonons are coherently annihilated or created in exchange for photons. Similar phenomena have recently been observed through phonon-cavity coupling—energy exchange between the modes of a single system mediated by intrinsic material nonlinearity[4,5]. This has so far been demonstrated primarily for bulk crystalline, high-quality-factor ($Q > 10^5$) mechanical systems operated at cryogenic temperatures. Here, we propose graphene as an ideal candidate for the study of such nonlinear mechanics. The large elastic modulus of this material and capability for spatial symmetry breaking via electrostatic forces is expected to generate a wealth of nonlinear phenomena[6], including tunable intermodal coupling. We have fabricated circular graphene membranes and report strong phonon-cavity effects at room temperature, despite the modest Q factor (~100) of this system. We observe both amplification into parametric instability (mechanical lasing) and the cooling of Brownian motion in the fundamental mode through excitation of cavity sidebands. Furthermore, we characterize the quenching of these parametric effects at large vibrational amplitudes, offering a window on the all-mechanical analogue of cavity optomechanics, where the observation of such effects has proven elusive.

Mechanical resonators composed of atomically thin membranes have been widely studied in recent years[7–16]. In the case of graphene, its low mass ($\rho_g \approx 0.75\,\mathrm{mg\,m^{-2}}$) electrical integrability and strong optical interaction[11,17] make it a rich and versatile system that has been studied largely for force and mass sensing. At room temperature the moderate Q factor, extreme frequency tunability and low in-line resistance of graphene resonators make them promising as intermediate-frequency (1–50 MHz) electromechanical elements, including passive filters and oscillators. At cryogenic temperatures ($T < 4$ K) graphene is becoming an attractive system for the study quantum motion, as it exhibits both large zero-point motion and a drastically enhanced Q-factor; progress towards this end has already been made[18–20], with coupling to on-chip microwave cavities and significant optomechanical cooling recently demonstrated. The mechanical nonlinearity studied here represents a complementary method for the parametric control of these membranes based on the intrinsic interactions of their vibrational modes. This effect can be utilized to enhance the Q-factor (and hence sensitivity) of graphene-based sensors, provide multimode readout through the detection of a single mode[21] and ultimately enable information exchange between optically cooled quantum modes. Moreover, this coupling makes graphene viable as low-power, tunable, electromechanical frequency mixers.

The primary source of nonlinearity in graphene membranes is motion-induced tension modulation. Similar to mode coupling in other mechanical systems[4,22,23], one vibrational mode (here assumed to be the fundamental mode at frequency ω_1) can be parametrically manipulated through its interaction with a second mode, which is deemed the phonon cavity (at ω_c). Exciting the coupled system at the cavity's red sideband ($\omega_c - \omega_1$) results in energy flow from the fundamental to the cavity mode, whereas pumping the blue sideband ($\omega_c + \omega_1$) generates amplification of both the fundamental and cavity modes; these processes are depicted in Fig. 1c. The efficiency of this intermodal energy exchange is dictated by the coupling rate $G = \mathrm{d}\omega_c/\mathrm{d}x_1$, where x_1 is the amplitude of motion at ω_1. This coupling rate is reminiscent of cavity optomechanics, and an identical formalism can be used to derive the resulting equations of motion (Supplementary Section 1).

The advantages of graphene over other membrane materials (such as SiN or MoS_2) in generating this effect are twofold. As will be shown below, G increases linearly with the static membrane deflection x_0. In typical graphene devices this value can be tuned electrostatically via a d.c. gate voltage. Moreover, graphene can withstand exceptionally large out-of-plane stretching as a result of its atomic thinness ($h \sim 0.3$ nm) and low in-plane stiffness $C = Eh/(1-\nu^2)$, where E and ν are the elastic modulus (160 GPa (ref. 24) to 1.0 TPa (ref. 25)) and Poisson's ratio respectively. Previous studies of suspended graphene have shown that x_0 can exceed 3% of the membrane width without rupturing[26]. As the tension in graphene is highly tunable, the frequency spectrum can be adjusted to obtain three-mode alignment, $\omega_c \pm \omega_1 \approx \omega_{sb}$. Here ω_{sb} signifies the resonance of a third mode that overlaps the cavity sideband and enhances pumping by a factor of Q_{sb}; this arrangement is also depicted in Fig. 1c. Under these conditions, it is thus possible to generate large phonon-cavity effects in the room-temperature graphene system.

Alternative intermodal coupling mechanisms for tensioned membranes do exist—most notably, mutual coupling to a resonance of the surrounding substrate[23]. Such systems enable parametric membrane control in a manner qualitatively similar to the coupling studied here, but also necessitate the three-mode alignment described above, which can be a challenge if the spectrum is not experimentally tunable. Moreover, a unique feature of the graphene system is the tunability of the coupling rate itself, $G \propto x_0$, which is present neither in the substrate-coupled case nor in standard optomechanical systems.

We have fabricated circular graphene drums with a diameter d ranging from 5–20 μm; we report measurements of two such drums—Device 1 ($d = 8$ μm) and Device 2 ($d = 20$ μm)—although the effects reported have been observed across a wide number of samples. A diagram of the experimental set-up and a micrograph of Device 1 are shown in Fig. 1a,b. Motion is driven electrostatically

[1]Department of Physics, Cornell University, Ithaca, New York 14853, USA. [2]Department of Physics, Nanoscience Center, University of Jyväskylä, Jyväskylä FI-40014, Finland. [3]School of Applied & Engineering Physics, Cornell University, Ithaca, New York 14853, USA. [4]Kavli Institute at Cornell for Nanoscale Science, Ithaca, New York 14853, USA. *e-mail: rd366@cornell.edu

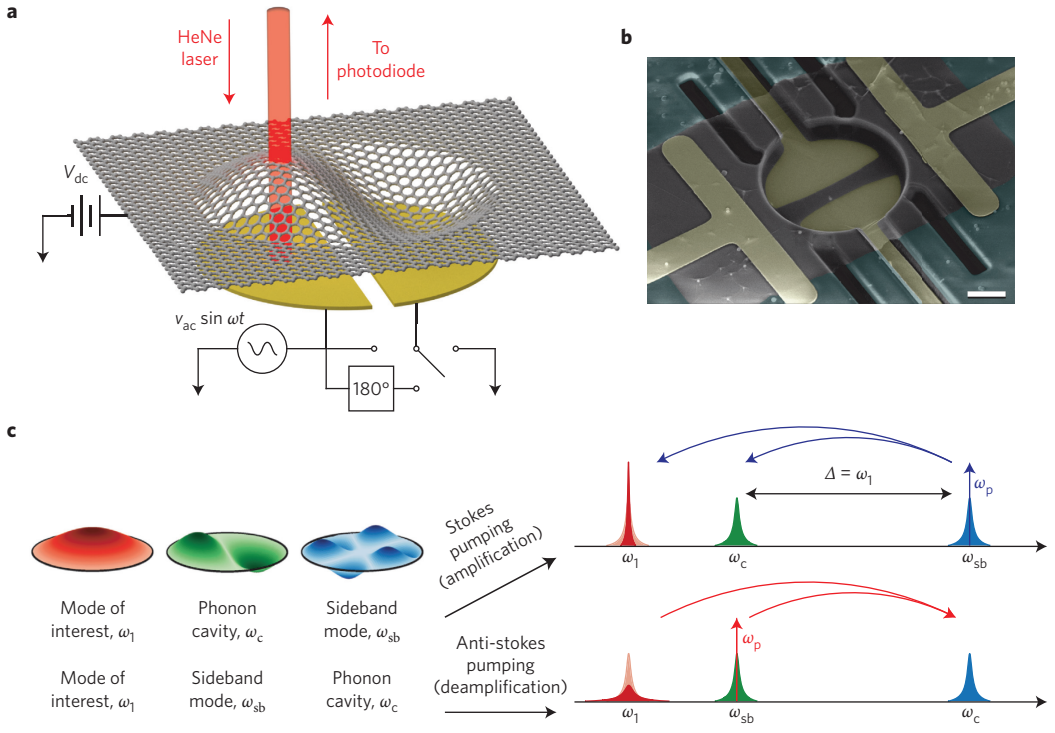

Figure 1 | The nonlinear system under test. a, A schematic of the experimental set-up. Graphene motion is driven electrostatically by two metallic back-gates and detected through optical interferometry. The gates can be driven in various configurations to favour excitation of the fundamental mode, higher-frequency modes or both. **b**, False-colour electron micrograph of Device 1. Scale bar, 2 μm. **c**, Schematic of the three modes necessary for efficient sideband pumping and their relative positions in frequency space. The curved arrows indicate the direction of energy flow when the system is pumped at ω_p.

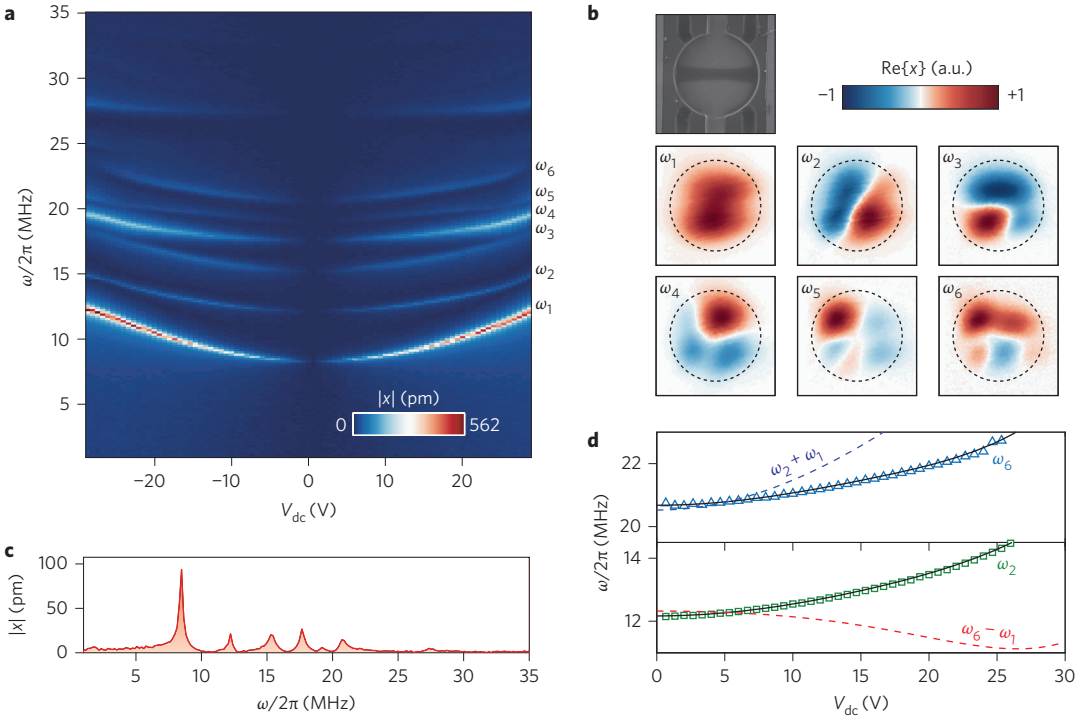

Figure 2 | Multimode membrane characterization. a, Frequency dispersion with V_{dc} for the lowest six modes in Device 1. **b**, Mechanical mode shapes at $V_{dc} = 5$ V measured by scanning the detection laser across the membrane surface while driving on resonance; colour denotes the real part of the complex amplitude x, that is, the quadrature of x that is 90° out of phase with the applied a.c. voltage. The electron micrograph is given as a reference for orientation. **c**, Frequency spectrum at $V_{dc} = 5$ V. **d**, Resonant frequencies of mode 2 and mode 6 extracted from **a** in comparison with their sidebands with mode 1. Appreciable overlap between these frequencies occurs for $V_{dc} = 0$–7.5 V and strong phonon-cavity effects are thus expected in this range.

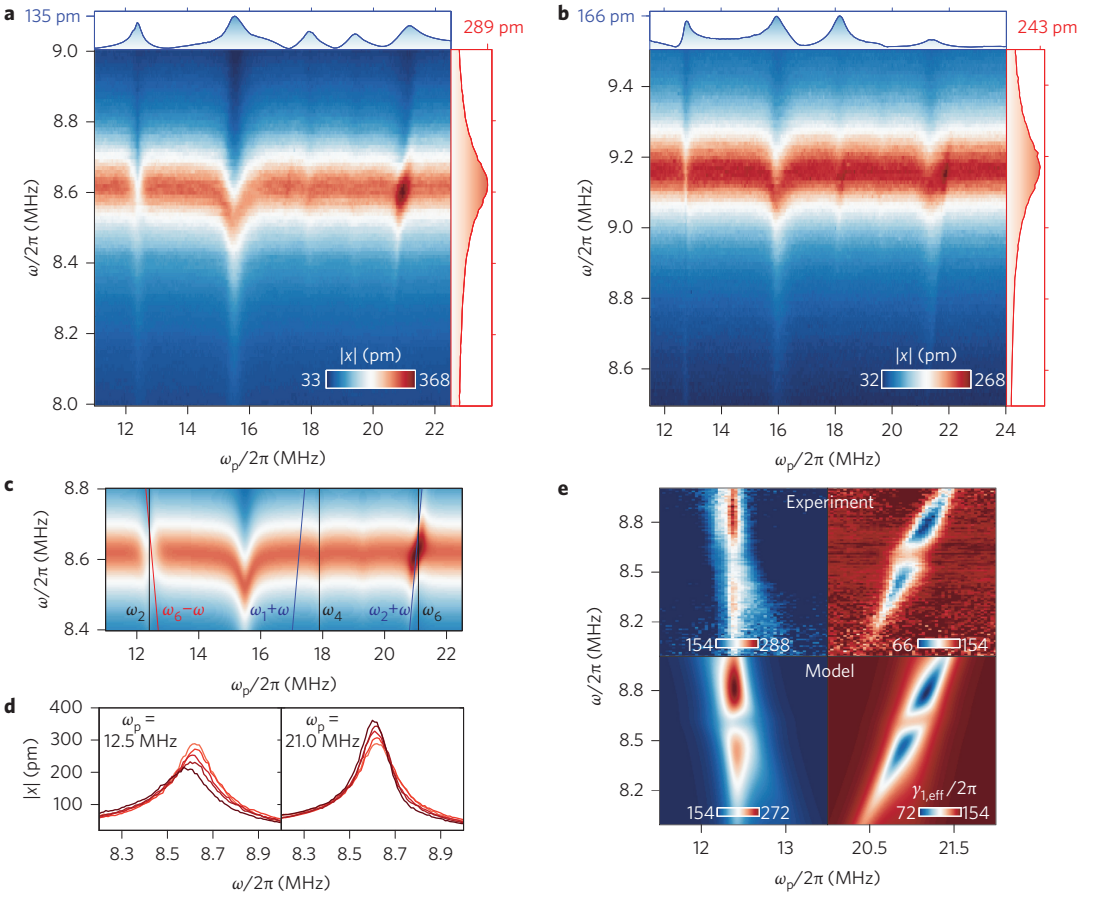

Figure 3 | Phonon pumping in Device 1. a,**b**, Mode 1 amplitude versus ω_p and ω at $V_{dc} = 5$ V (**a**) and 10 V (**b**). Right panels: Vertical slices through the data at the highest ω_p value. Upper panels: Motion in the membrane at ω_p measured simultaneously with the main panel. Measurements for both V_{dc} values were performed with equal excitation forces ($F \propto V_{dc}v_{ac}$) at the pump frequency; probe frequency forces were also equal. Cavity amplification and deamplification of mode 1 are stronger in **a**, where there is better mode–sideband alignment. **c**, Modelled behaviour in **a** based on equations (2)–(4). Solid lines denote the relevant frequencies for sideband effects. **d**, Measured response at the cavity sidebands for $V_{dc} = 5$ V with linearly increasing pump strength (darkening lines). **e**, Effective mode 1 damping as measured in **a** (top) and modelled by equation (3) (bottom) expressed in kHz (colour scales). The colours in the upper panel are truncated to the intrinsic damping $\gamma_1/2\pi = 154$ kHz. Quenching of the cavity effect near $\omega = \omega_1$ is due to the large mode 1 amplitude and a non-zero $T_{sb,c}$ coupling. Only two free parameters (T_{1c} and $T_{sb,c}$) were used to produce each of the lower panels.

via an applied gate voltage $V_{dc} + v_{ac} \sin \omega t$ (where ω, t denote the drive frequency and time, respectively), and detected optically through laser interferometry[11]. Unlike previous generations of graphene resonators, our structures feature two independent back-gates that enable efficient actuation of several modes. The gate–graphene separation is 1.7 μm. Most measurements were performed with one gate grounded and a drive voltage applied to the other, although other configurations (shown in Fig. 1a) can be used to favour either the fundamental or higher modes.

Device 1 has six modes that can be readily excited (Fig. 2a,b). The frequency dispersion of this spectrum with V_{dc} is shown in Fig. 2a. Between $V_{dc} = 0$–7.5 V, there is significant overlap of modes 1, 2, 6 and their respective sidebands (Fig. 2d); therefore this is where we expect the strongest phonon-cavity effect. At $V_{dc} = 5$ V the graphene has natural frequencies and Q-factors of: $\omega_1/2\pi = 8.6$ MHz, $\omega_2/2\pi = 12.4$ MHz, $\omega_6/2\pi = 21.0$ MHz, $Q_1 = \omega_1/\gamma_1 = 57$, $Q_2 = 48$ and $Q_6 = 37$.

The general Hamiltonian for two coupled modes in a uniformly tensioned membrane is

$$H = \sum_{n=i,j}\left(\frac{p_n^2}{2m} + \frac{1}{2}m\omega_n^2 x_n^2 + L_n x_n + S_n x_n^2 + T_n x_n^3 + F_n x_n^4\right) + T_{ij}x_i x_j^2 + T_{ji}x_j x_i^2 + F_{ij}x_i^2 x_j^2 \quad (1)$$

where m and p_n are the membrane mass and momentum of mode n; a derivation of equation (1) can be found in Supplementary Section 1. The fourth-order nonlinearity F_i is the stretching-induced Duffing term and is proportional to the membrane stiffness C. The remaining terms L_i, S_i and T_i originate from the same geometric nonlinearity as F_i, combined with a static displacement x_0. Although the exact derivation requires the full solution of the elastic problem for the membrane, L_i, S_i and T_i can be viewed roughly as resulting from a binomial expansion of $F_i(x_0 + x_i \cos \omega_i t)^4$. The coupling terms F_{ij} and T_{ij} have similar origins, resulting in $T_{ij} \propto x_0$. In the Supplementary Information we present a calculation of these nonlinear coefficients for circular membranes and for a general membrane geometry.

To understand how each term in equation (1) influences membrane mechanics, it is useful to consider the forces acting on mode i ($-\partial H/\partial x_i$) and examine each term in isolation. Using this approach we see that L_i has no effect other than to exert a constant force on mode i, whereas S_i modifies the linear spring constant $m\omega_i^2$ and T_i and F_i contribute to a nonlinear spring constant. The coupling term F_{ij} alters the mode i spring constant by an amount proportional to $|x_j|^2$. Only the third-order term T_{ij} generates a phonon-cavity effect on mode i. This is a result of its combined influence on i and j: if mode i is driven at ω_i while mode j is driven at $\omega_j \pm \omega_i$, mode j experiences a force $T_{ij}x_i x_j \propto \cos \omega_j t$, which produces motion at the cavity resonance ω_j. The two frequency

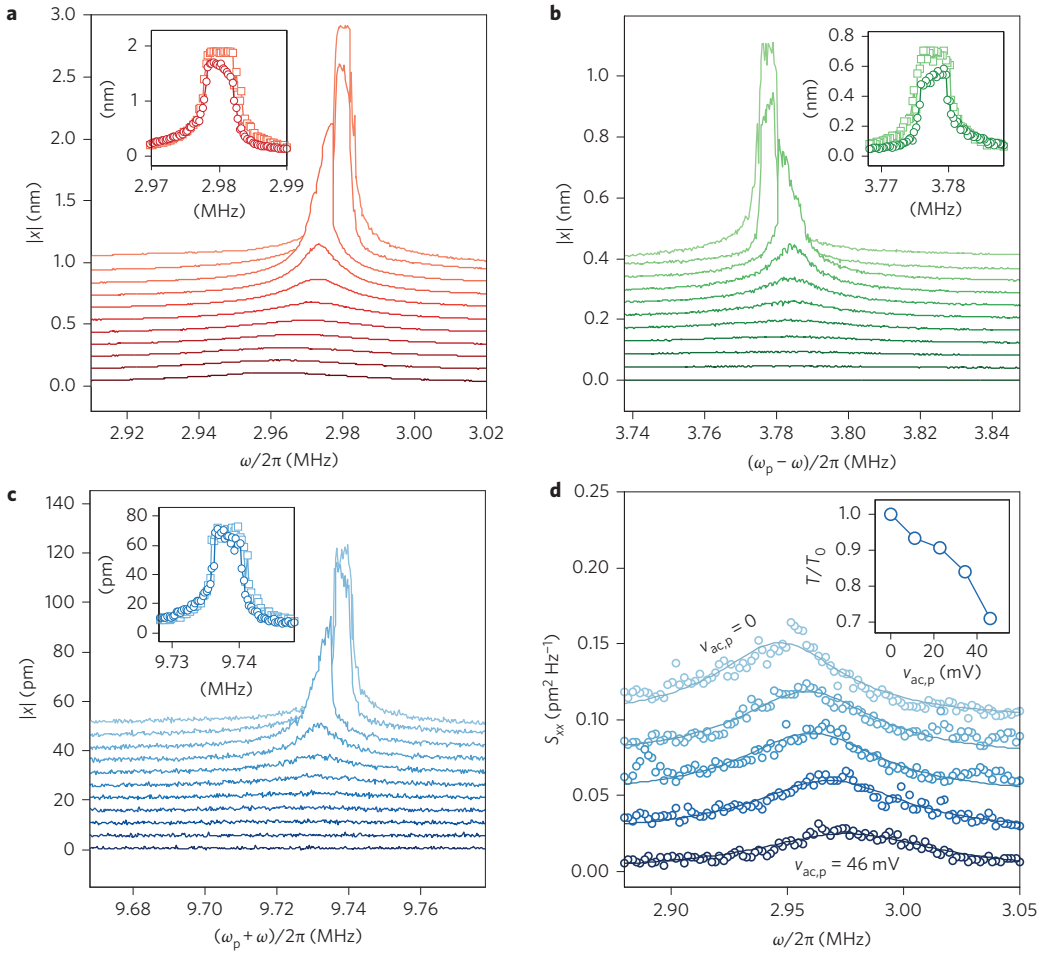

Figure 4 | Parametric self-oscillation and cooling in Device 2. a, Amplification of mode 1 ($\omega_1/2\pi = 3.0$ MHz, $\gamma_1/2\pi = 45$ kHz) and the transition to mechanical lasing ($\gamma_{1,\mathrm{eff}} \leq 0$) via mode coupling. Mode 1 is probed with a weak drive ($v_{\mathrm{ac}} = 0.4$ mV) as mode 2 is pumped at its Stokes sideband ($\omega_{\mathrm{p}} = 6.8$ MHz) with increasing pump strength ($v_{\mathrm{ac,p}} = 0$–400 mV). The curves are vertically offset for clarity. Inset: Saturation of the vibrational amplitude and the flat-top response of the self-oscillating mode; no vertical offset is applied. **b**,**c**, Frequency mixing via mechanics. Measured membrane motion at $\omega_p - \omega$ (**b**) and $\omega_p + \omega$ (**c**) recorded simultaneously with **a**. **d**, Measured spectral noise density near ω_1 on pumping the anti-Stokes sideband of mode 5 ($\omega_{\mathrm{p}} = 3.8$ MHz). The curves are vertically offset for clarity. Inset: the effective temperature of mode 1 (normalized by $T_0 = 293$ K), corresponding to the area under the S_{xx} fits. The frequency spectrum of Device 2 is given in Supplementary Section 2.

components of j then mix to exert a back-action force $T_{ij}x_j^2 \propto \cos\omega_i t$ on mode i, which will amplify or dampen its motion depending on the phase of this force (that is, whether the + or − sideband was driven). The remaining term T_{ji} has no appreciable impact on mode i, but enables cavity effects on mode j.

Referring again to i and j as modes 1 and c, the cavity coupling rate (in a linearized approximation) is $G = \mathrm{d}\omega_c/\mathrm{d}x_1 \approx T_{1c}/m\omega_c$. To measure this coupling we drive our graphene membrane with a probe signal at frequency $\omega \approx \omega_1$ and a pump signal at ω_{p}. In terms of the cavity detuning $\Delta = \omega_{\mathrm{p}} - \omega_{\mathrm{c}}$ and the pumped vibration amplitude x_{p}, the effective resonant frequency and damping of mode 1 are:

$$\omega_{1,\mathrm{eff}} = \Omega_1 + \frac{2G^2|x_{\mathrm{p}}|^2\Delta[\gamma_{\mathrm{c}}^2/4 - \omega^2 + \Delta^2]}{[\gamma_{\mathrm{c}}^2/4 + (\omega-\Delta)^2][\gamma_{\mathrm{c}}^2/4 + (\omega+\Delta)^2]} \quad (2)$$

$$\gamma_{1,\mathrm{eff}} = \gamma_1 - \frac{4G^2|x_{\mathrm{p}}|^2\gamma_{\mathrm{c}}\Delta\Omega_1}{[\gamma_{\mathrm{c}}^2/4 + (\omega-\Delta)^2][\gamma_{\mathrm{c}}^2/4 + (\omega+\Delta)^2]} \quad (3)$$

$$m\omega_1\Omega_1 = m\omega_1^2 + 2S_1 - 12\frac{T_1(T_{1\mathrm{c}}|x_{\mathrm{p}}|^2 + L_1/2)}{m\omega_1^2 + 4S_1} + 4F_{1\mathrm{c}}|x_{\mathrm{p}}|^2 \quad (4)$$

where Ω_1 describes the combined effects of L_1, S_1, T_1 and $F_{1\mathrm{c}}$ on the mode 1 spring constant.

The vibration amplitude of Device 1, mode 1 is shown in Fig. 3a,b as ω_{p} is swept from ω_2 to ω_6. The $|x_{\mathrm{p}}|^2$ terms in equation (4) generate a downward frequency shift when any mode is pumped directly on resonance; this is most visible at $\omega_{\mathrm{p}}/2\pi \approx 16$ MHz. Sideband amplification and deamplification are also seen and occur when pumping the blue sideband of mode 2 and red sideband of mode 6, respectively (Fig. 3a). Amplification also occurs at $\omega_{\mathrm{p}} = 2\omega_1$ and is most notable at $V_{\mathrm{dc}} = 10$ V, where $2\omega_1 \approx \omega_4$; this effect is studied in further detail in Supplementary Section 5.

The amplitude of mode 1 on sideband pumping, shown in Fig. 3d, is nearly linear with pump amplitude—in contrast to the $|x_{\mathrm{p}}|^2$ dependence predicted by equation (3). Analysing the effective damping $\gamma_{1,\mathrm{eff}}$ at the cavity sidebands reveals the source of this disagreement (Fig. 3e). Suppression of the sideband effects is observed around $\omega = \omega_1$, indicating a broadening of the sideband mode due to the probe amplitude x_1. For the case of $\omega_{\mathrm{c}} = \omega_2$, $\omega_{\mathrm{sb}} = \omega_6$, motion at ω_1 and a non-zero coupling T_{62} result in increased mode 6 damping $\gamma_{6,\mathrm{eff}}$, hindering its ability to amplify mode 1. This quenching of the cavity effects can be avoided by probing mode 1 with lower amplitudes and speaks to the dynamic range of a micromechanical filter/amplifier based on phonon-cavity coupling. Careful engineering of the device modes

such that $T_{sb,c} \approx 0$ would counteract this effect, and can potentially be achieved by using a more sophisticated membrane clamping scheme[27] or altering the membrane shape[28]. A detailed analysis of this quenching is presented in Supplementary Section 6. Correcting for this effect (Supplementary Fig. 8) shows that the coupling rates in this device are $G = 6$ MHz nm^{-1} for blue sideband pumping (amplification) and $G = 8$ MHz nm^{-1} for red sideband pumping (deamplification). At the single quantum level, these correspond to $g_0 = G|x_{1,zpm}| = 300$ Hz and $g_0 = 400$ Hz respectively, where $x_{1,zpm} = \sqrt{(\hbar/2m\omega_1)}$ is the zero-point motion of mode 1.

Stronger phonon-cavity effects have been measured in Device 2, where the larger device diameter permits the use of much weaker probe signals while maintaining comparable signal/noise ratios. Measurements were performed with $V_{dc} = 4$ V, so that $\omega_1 + \omega_2 \approx \omega_5$. Figure 4a shows the membrane response on pumping at $\omega_p = \omega_1 + \omega_2 = 2\pi \times 6.76$ MHz with an a.c. voltage $v_{ac,p}$ ramped linearly from 0–400 mV. Mode 1 is probed with $v_{ac} = 0.4$ mV and its motion undergoes amplification by a factor of 8.5 (19 dB) before entering instability ($\gamma_{1,eff} \leq 0$) at $v_{ac,p} = 300$ mV. Above this pump strength, mode 1 undergoes self-oscillation and locks onto the probe signal with a flat frequency response. The width of this flat region is 4 kHz, significantly narrower than the unpumped linewidth $\gamma_1/2\pi = 45$ kHz. Amplification of mode 1 continues to rise for higher pump strengths, reaching a factor of 18 (25 dB) at the highest value tested.

In this configuration the graphene membrane also acts as a frequency mixer, generating motion at $\omega_p + \omega$ and $\omega_p - \omega$ (Fig. 4b–c). Motion at $\omega_p - \omega \approx \omega_2$ signifies occupation of the cavity mode as a result of down-scattered pump phonons, and so is significantly larger (10×) than motion at $\omega_p + \omega$, where there is no mechanical resonance. Both of these mixed tones inherit the flat-top spectrum of mode 1 when it is in the self-oscillating regime.

Similar to deamplification in Device 1, red sideband pumping in Device 2 has been used to cool the thermal motion of mode 1 to 208 K (Fig. 4d). As in previous phonon-cavity studies[4], the low cavity frequency $\omega_c \sim \omega_1$ (and high thermal phonon occupation) limits cooling in the all-mechanical system. Cooling motion towards the quantum ground state thus remains a task best suited for optical/microwave cavities, where $\omega_c \gg \omega_1$. However, interesting prospects arise if optical cavities and phonon cavities are utilized simultaneously to control graphene motion. For instance, optically cooling the phonon cavity enhances its capacity to mechanically cool the fundamental mode—in such a case cooling is limited only by the cooperativities $G^2|x_p|^2/\gamma_1\gamma_c$ of the two cavities. Moreover, the mechanical pump grants experimental control over the interaction strength of the two modes. Microwave-cavity-coupled graphene systems[18–20] are therefore ideal testbeds for quantum entanglement, squeezing, thermalization and information exchange between modes near their ground state. The greatly enhanced Q-factors of graphene at dilution refrigerator temperatures[8,29] will only serve to strengthen these effects.

We have demonstrated tension-mediated coupling between mechanical modes in suspended graphene and its potential for parametric control of this system. Sideband cooling and the amplification of membrane motion up to self-oscillation have been observed within a single device. The potential for graphene membranes to be used as frequency mixers with intrinsically flat pass-bands has also been shown. As graphene, transition metal dichalcogenides and related two-dimensional materials continue to be developed and exploited for their unique mechanical properties, these inherent membrane nonlinearities can ultimately be used to artificially enhance the Q-factors of future sensors and electronics, to facilitate bitwise logic operations between coupled membrane modes[30] and to open new possibilities in the study of coupled quantum systems.

Methods

Methods and any associated references are available in the online version of the paper.

Received 18 November 2015; accepted 26 April 2016; published online 13 June 2016

References

1. O'Connell, A. D. *et al.* Quantum ground state and single-phonon control of a mechanical resonator. *Nature* **464,** 697–703 (2010).
2. Teufel, J. D. *et al.* Sideband cooling of micromechanical motion to the quantum ground state. *Nature* **475,** 359–363 (2011).
3. Andrews, R. W. *et al.* Bidirectional and efficient conversion between microwave and optical light. *Nature Phys.* **10,** 321–326 (2014).
4. Mahboob, I., Nishiguchi, K., Okamoto, H. & Yamaguchi, H. Phonon-cavity electromechanics. *Nature Phys.* **8,** 387–392 (2012).
5. Mahboob, I., Nishiguchi, K., Fujiwara, A. & Yamaguchi, H. Phonon lasing in an electromechanical resonator. *Phys. Rev. Lett.* **110,** 127202 (2013).
6. Khan, R., Massel, F. & Heikkilä, T. T. Tension-induced nonlinearities of flexural modes in nanomechanical resonators. *Phys. Rev. B* **87,** 235406 (2013).
7. Bunch, J. S. *et al.* Electromechanical resonators from graphene sheets. *Science* **315,** 490–493 (2007).
8. Chen, C. *et al.* Performance of monolayer graphene nanomechanical resonators with electrical readout. *Nature Nanotech.* **4,** 861–867 (2009).
9. Singh, V. *et al.* Probing thermal expansion of graphene and modal dispersion at low-temperature using graphene nanoelectromechanical systems resonators. *Nanotechnology* **21,** 165204 (2010).
10. Chaste, J. *et al.* A nanomechanical mass sensor with yoctogram resolution. *Nature Nanotech.* **7,** 301–304 (2012).
11. Barton, R. A. *et al.* Photothermal self-oscillation and laser cooling of graphene optomechanical systems. *Nano Lett.* **12,** 4681–4686 (2012).
12. Song, X. *et al.* Stamp transferred suspended graphene mechanical resonators for radio frequency electrical readout. *Nano Lett.* **12,** 198–202 (2012).
13. Eichler, A. *et al.* Nonlinear damping in mechanical resonators made from carbon nanotubes and graphene. *Nature Nanotech.* **6,** 339–342 (2011).
14. Eichler, A., del Álamo Ruiz, M., Plaza, J. A. & Bachtold, A. Strong coupling between mechanical modes in a nanotube resonator. *Phys. Rev. Lett.* **109,** 025503 (2012).
15. Lee, J., Wang, Z., He, K., Shan, J. & Feng, P. X.-L. High frequency MoS_2 nanomechanical resonators. *ACS Nano* **7,** 6086–6091 (2013).
16. Liu, C. H., Kim, I. S. & Lauhon, L. J. Optical control of mechanical mode-coupling within a MoS_2 resonator in the strong-coupling regime. *Nano Lett.* **15,** 6727–6731 (2015).
17. Cole, R. M. *et al.* Evanescent-field optical readout of graphene mechanical motion at room temperature. *Phys. Rev. Appl.* **3,** 1–7 (2015).
18. Weber, P., Güttinger, J., Tsioutsios, I., Chang, D. E. & Bachtold, A. Coupling graphene mechanical resonators to superconducting microwave cavities. *Nano Lett.* **14,** 2854–2860 (2014).
19. Song, X., Oksanen, M., Li, J., Hakonen, P. J. & Sillanpää, M. A. Graphene optomechanics realized at microwave frequencies. *Phys. Rev. Lett.* **113,** 1–5 (2014).
20. Singh, V. *et al.* Optomechanical coupling between a graphene mechanical resonator and a superconducting microwave cavity. *Nature Nanotech.* **9,** 1–5 (2014).
21. Atalaya, J., Kinaret, J. M. & Isacsson, A. Narrowband nanomechanical mass measurement using nonlinear response of a graphene membrane. *Europhys. Lett.* **91,** 48001 (2009).
22. Westra, H. J. R., Poot, M., van der Zant, H. S. J. & Venstra, W. J. Nonlinear modal interactions in clamped-clamped mechanical resonators. *Phys. Rev. Lett.* **105,** 117205 (2010).
23. Patil, Y. S., Chakram, S., Chang, L. & Vengalattore, M. Thermomechanical two-mode squeezing in an ultrahigh Q membrane resonator. *Phys. Rev. Lett.* **115,** 017202 (2015).
24. Ruiz-Vargas, C. S. *et al.* Softened elastic response and unzipping in chemical vapor deposition graphene membranes. *Nano Lett.* **11,** 2259–2263 (2011).
25. Lee, C., Wei, X., Kysar, J. W. & Hone, J. Measurement of the elastic properties and Intrinsic strength of monolayer graphene. *Science* **321,** 385–388 (2008).
26. Bunch, J. S. *et al.* Impermeable atomic membranes from graphene sheets. *Nano Lett.* **8,** 2458–2462 (2008).
27. Lee, S. *et al.* Electrically integrated SU-8 clamped graphene drum resonators for strain engineering. *Appl. Phys. Lett.* **102,** 153101 (2013).
28. Wang, Z., Lee, J., He, K., Shan, J. & Feng, P. X.-L. Embracing structural nonidealities and asymmetries in two-dimensional nanomechanical resonators. *Sci. Rep.* **4,** 3919 (2014).
29. Van Der Zande, A. M. *et al.* Large-scale arrays of single-layer graphene resonators. *Nano Lett.* **10,** 4869–4873 (2010).
30. Mahboob, I. & Yamaguchi, H. Bit storage and bit flip operations in an electromechanical oscillator. *Nature Nanotech.* **3,** 275–279 (2008).

Acknowledgements

The authors are grateful to P. Rose for assistance in growing the CVD graphene and to D. MacNeill for insightful discussions and comments. This work was supported by the

Cornell Center for Materials Research with funding from the NSF MRSEC program (grant no. DMR-1120296) and by Nanoelectronics Research Initiative (NRI) through the Institute for Nanoelectronics Discovery and Exploration (INDEX). Support was also provided by the Academy of Finland (through the project 'Quantum properties of optomechanical systems'). Fabrication was performed in part at the Cornell NanoScale Facility, a member of the National Nanotechnology Coordinated Infrastructure, which is supported by the NSF (grant no. ECCS-15420819).

Author contributions

J.M.P., H.G.C., P.L.M. and R.D.A. designed the experiment; F.M. developed the supporting theory. R.D.A. and T.S.A. fabricated the samples; I.R.S. contributed to the design of the samples and the experimental set-up. R.D.A. and A.H. carried out the measurements. F.M. and R.D.A. analysed the data. All authors discussed the results and commented on the manuscript.

Additional information

Supplementary information is available in the online version of the paper. Reprints and permissions information is available online at www.nature.com/reprints. Correspondence and requests for materials should be addressed to R.D.A.

Competing financial interests

The authors declare no competing financial interests.

Methods

Mechanical resonators were fabricated by the growth of monolayer graphene through chemical vapour deposition and transfer to pre-patterned substrates. Before transfer, a supporting layer of 150 nm poly-methyl-methacrylate (PMMA) was spin-coated on the graphene surface and cured at 170 °C. During the transfer the Cu growth substrate was etched using $FeCl_3$ and the PMMA/graphene film was cleaned by soaking in a series of deionized water baths. After transfer, the film was coated with photoresist and patterned via optical lithography; the resist and PMMA were removed by submersion in *N*-methyl-2-pyrollidine at 80 °C, releasing the suspended graphene membranes.

All measurements were performed at room temperature in a vacuum of $P < 10^{-6}$ mbar. The detection of mechanical motion was performed through optical interferometry, as detailed in previous work[11], using 190 μW and 130 μW of incident laser power for Devices 1 and 2, respectively. The light source used was an HeNe 633 nm laser, focused to a spot of diameter ~1 μm. Reflected light was monitored by a high-frequency photodetector (New Focus 1811-FS) and recorded using a multichannel lock-in amplifier (Zurich Instruments HF2LI). The same lock-in amplifier was used to supply excitation voltages at the pump and probe frequencies. Graphene motion was inferred from the modulated laser power using the optical calibration scheme detailed in Supplementary Section 3.